Nuclear Engineering and Technology 50 (2018) 416–424

Contents lists available at ScienceDirect

Nuclear Engineering and Technology

journal homepage: www.elsevier.com/locate/net

Original Article

Microscopic characterization of pretransition oxide formed on Zr–Nb–Sn alloy under various Zn and dissolved hydrogen concentrations

Sungyu Kim [a], Taeho Kim [b], Ji Hyun Kim [b], Chi Bum Bahn [a, *]

[a] School of Mechanical Engineering, Pusan National University, Busan 46241, Republic of Korea
[b] Department of Nuclear Engineering, School of Mechanical, Aerospace and Nuclear Engineering, Ulsan National Institute of Science and Technology (UNIST), Ulsan 44919, Republic of Korea

ARTICLE INFO

Article history:
Received 15 March 2017
Received in revised form
17 November 2017
Accepted 22 November 2017
Available online 12 December 2017

Keywords:
Dissolved Hydrogen Effect
Porosity
Pretransition Oxide
Transmission Electron Microscopy (TEM)
Zirconium Alloys

ABSTRACT

Microstructure of oxide formed on Zr–Nb–Sn tube sample was intensively examined by scanning transmission electron microscopy after exposure to simulated primary water chemistry conditions of various concentrations of Zn (0 or 30 ppb) and dissolved hydrogen (H_2) (30 or 50 cc/kg) for various durations without applying desirable heat flux. Microstructural analysis indicated that there was no noticeable change in the microstructure of the oxide corresponding to water chemistry changes within the test duration of 100 days (pretransition stage) and no significant difference in the overall thickness of the oxide layer. Equiaxed grains with nano-size pores along the grain boundaries and microcracks were dominant near the water/oxide interface, regardless of water chemistry conditions. As the metal/oxide interface was approached, the number of pores tended to decrease. However, there was no significant effect of H_2 concentration between 30 cc/kg and 50 cc/kg on the corrosion of the oxide after free immersion in water at 360°C. The adsorption of Zn on the cladding surface was observed by X-ray photoelectron spectroscopy and detected as ZnO on the outer oxide surface. From the perspective of OH^- ion diffusion and porosity formation, the absence of noticeable effects was discussed further.

1. Introduction

The corrosion of zirconium fuel cladding is known to limit the lifetime and cycle of reloading of fuel in a reactor. Therefore, extensive research has been conducted to better understand the corrosion mechanism and degradation of zirconium fuel cladding under various high-temperature water chemistry conditions. However, there is still no clear understanding of the oxide growth mechanism related to cladding integrity. The corrosion kinetics of zirconium alloy has been widely known to consist of three stages: pretransition, transitory, and posttransition [1]. It has been proposed that accumulated stress, which causes the formation of cracks in the oxide, contributes to the transition in corrosion kinetics [2]. In addition, crack initiation has been linked to the metal/oxide interface roughness [3,4]. Parise et al. showed the stress distribution of the undulated interface through metal–oxide system modeling during zirconium alloy oxidation [5]. Some researchers have suggested that lateral cracks act as obstacles to the diffusion of oxidizing species [6], whereas others assume that they act as easy diffusion paths through surface diffusion [7]. Other researchers have recently suggested that the interconnection of porosity from the water/oxide interface to the metal/oxide interface is a key mechanism for the transition in corrosion kinetics [8]. Ploc found three kinds of pores, flake, ribbon, and stress cracks, in Zr–2.5Nb samples corroded under heavy water coolant condition [9]. Bossis et al. reported a porous outer layer in a pretransition oxide analyzed by secondary ion mass spectrometry and electrical impedance spectroscopy [3]. Cox anticipated that porosity would provide connected paths between the external oxidizing medium and the underlying metal [10]. Gong et al. reported nanopores in strings formed on Zr–Nb–Y alloy and N18 alloy (Zr – 0.39Nb – 0.93Sn – 0.31Fe – 0.08Cr – 0.048O, wt%) at grain boundaries and suggested that the initiation mechanism of porosity is due to the Kirkendall effect [11].

Recent research on the oxidation of Zr alloys appears to focus on the suboxide [8,12–14] and segregation of minor elements, such as

* Corresponding author.
E-mail address: bahn@pusan.ac.kr (C.B. Bahn).

https://doi.org/10.1016/j.net.2017.11.009

Fe, at the interface [12], as well as porosity formation. The oxide phases that exist near the metal/oxide interface appear rather complex, suggesting the presence of a suboxide layer [8,12–14]. A large variation in the width of the ZrO suboxide phase at different metal/oxide interface locations has been observed, suggesting that oxidation is an extremely local process [8]. The segregation of minor elements has been observed using atom probe tomography [12]. The segregation along the interface, including grain boundaries, may affect the corrosion process of the Zr alloy.

Despite these recent research trends, however, studies of the oxidation of Zr alloy that have considered H_2 concentration and Zn injection are insufficient. Zn injection and adjusting the dissolved H_2 concentration have been considered as measures to alleviate the radiation buildup and to reduce cracking in nickel-based alloys [15–19]. However, the effect of these water chemistry modifications on nuclear fuel cladding oxidation, especially in a pressurized water reactor (PWR), has not been systematically studied yet. Wells et al. reported that for zirconium fuel cladding and spacer weld materials, the oxide growth rate was not affected by the different dissolved H_2 levels they applied [20]. Kass presented the hydrogen pickup of Zircaloy-4 as a function of hydrogen overpressure [21]. Yoon et al. reported the results of the oxide thickness of the fuel cladding in the Hanul unit 1 domestic nuclear power plant operated under Zn injection condition and showed that a 5-ppb Zn injection had no noticeable effects on the corrosion kinetics of the fuel cladding [22]. However, earlier studies have not provided detailed microstructural analyses of oxides. The main purpose of this study is to investigate the effects of Zn injection and H_2 concentration on the microstructure of the oxide layer formed on Zr–Nb–Sn alloy in simulated PWR primary water chemistry conditions. Assuming that the effects of Zn injection, if there are any, will be noticeable at the initial stage of oxidation, the pretransition oxides formed under the Zn injection condition from the beginning were analyzed. The results can provide better insight into the effects of Zn and H_2 concentrations on the corrosion mechanism of zirconium fuel cladding.

2. Experimental methods

Specimens of Zr–Nb–Sn alloy tubes were oxidized in an autoclave connected to a recirculation water loop at 360°C and 20 MPa for 300 hours, 50 days, and 100 days under simulated primary water chemistry conditions (pure H_2O with dissolved H_2 of 30 cc/kg, dissolved oxygen of 0–5 ppb, 2 ppm of Li^+ as LiOH, and 1200 ppm of B^{3+} as H_3BO_3). Dissolved H_2 was measured using an Orbisphere 31250 hydrogen sensor (Hach inc., Loveland, CO, USA), and dissolved oxygen (O_2) was measured using a Mettler Toledo 52-201-067 oxygen sensor (Mettler-Toledo International Inc., Greifensee, Switzerland) in outlet water at room temperature. The pressure difference between the interior and exterior of the cladding sample was maintained at 11.7 MPa by pressurizing argon (Ar) gas to 4.56 MPa at room temperature during exposure in the recirculation loop to simulate the compressive stress condition in the actual fuel cladding. A total of 30 ppb of Zn was injected only into 30 cc/kg of H_2 water. Zinc acetate dehydrate, $Zn(CH_3COO)_2$, was used to adjust the Zn concentration to 30 ppb. The Zn solution in the solution column was purged by Ar gas and then was injected into a one-through type primary water loop system. The comprehensive experimental conditions are shown in Table 1. The dimensions of the test samples were 9.5 mm in outer diameter, 0.6 mm in wall thickness, and 130 mm in length. The nominal chemical compositions of the test sample and the Zr–0.66Sn alloy sample [23] are shown in Table 2 for comparison with the thickness results. All tests were performed without applying heat flux or addition of impurities such as Ni or Fe oxide particulates to form the crud on the test specimen.

Table 1
Experimental conditions.

Experimental condition	Reference condition	High hydrogen	With Zn injection
Temperature	360°C	360°C	360°C
Pressure	20 MPa	20 MPa	20 MPa
Pressure difference between exterior and interior	11.7 MPa	11.7 MPa	11.7 MPa
Hydrogen	30 cc/kg	50 cc/kg	30 cc/kg
Li (LiOH)	2 ppm	2 ppm	2 ppm
B (H_3BO_3)	1,200 ppm	1,200 ppm	1,200 ppm
Zn [$Zn(CH_3COO)_2$]	None	None	30 ppb

Table 2
Chemical composition of the specimen used in this study and Wei et al. [23].

Specimens	Nb	Sn	Fe	O	C	N	Hf	Zr
This study	0.96	0.76	0.18	0.62	0.1	0.03	0.002	Bal.
Wei et al. [23]	0.91	0.66	0.09	–	–	–	–	Bal.

(Unit: wt%)

After immersion for a given duration and drying of the test specimens in air at room temperature, a thin layer of platinum was sputtered in vacuum on the outer oxide surface to protect the oxide layer formed under the given test conditions; then, *in situ* lift-out focused ion beam sectioning was carried out with an FEI Quanta 3D FEG instrument (FEI inc., Hillsboro, OR, USA) operated at 2–30 kV, with currents between 1 pA and 65 nA, to prepare thin foils for microstructural analysis of the oxide layer by transmission electron microscopy (TEM). Cs-corrected scanning transmission electron microscopy (STEM) observations were carried out with a JEOL JEM-ARM200F (JEOL inc., Akishima, Tokyo, Japan) operated at 200 kV. The composition of the precipitates was characterized by energy dispersive X-ray spectroscopy (EDS) elemental mapping. X-ray diffraction (XRD) measurements were also conducted with cross sections of samples using a Bruker D8 ADVANCE instrument (Bruker inc., Billerica, MA, USA) to characterize crystal structures. To investigate the interaction between Zn and oxide on the surface of the samples, X-ray photoelectron spectroscopy (XPS) surface analysis was conducted (Thermo Fisher Scientific K-Alpha+). The X-ray beam was incident on the surface of the samples in a 400 μm × 400 μm field area and was analyzed within 10 nm of depth. The thickness of the oxide layer was determined through STEM images. For the sample corroded for 100 days and having an increased interface roughness, the thickness was determined using

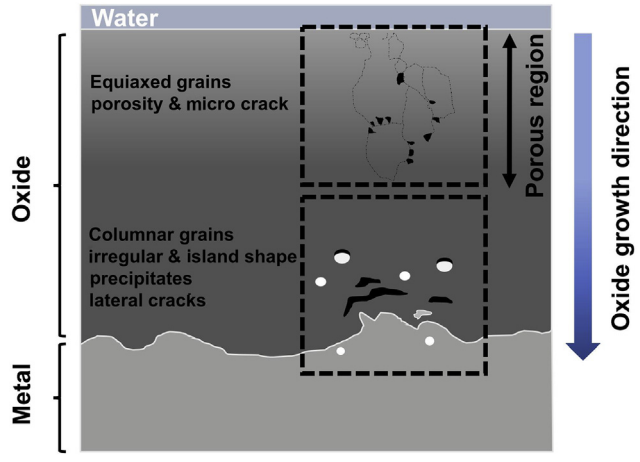

Fig. 1. Schematic diagram of the zirconium oxide layer.

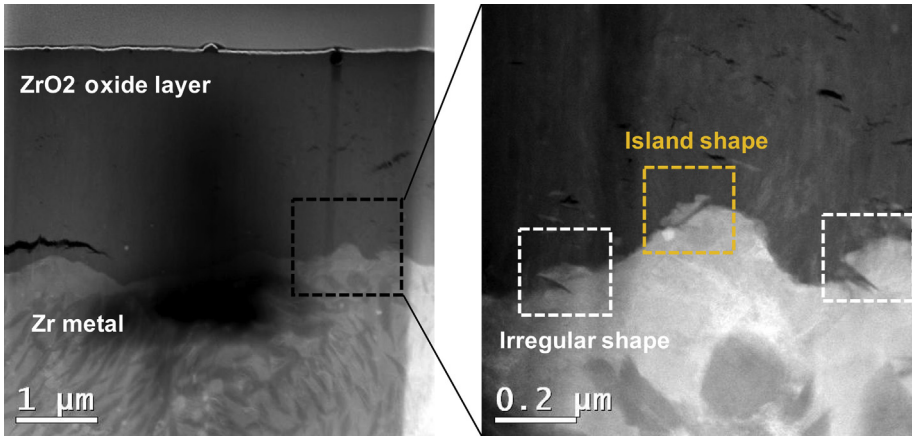

Fig. 2. High angle annular darkfield STEM image of the metal/oxide interface showing the irregular shape and island shape interface (100-day corroded sample in reference condition, 30 cc/kg H_2 concentration without Zn).

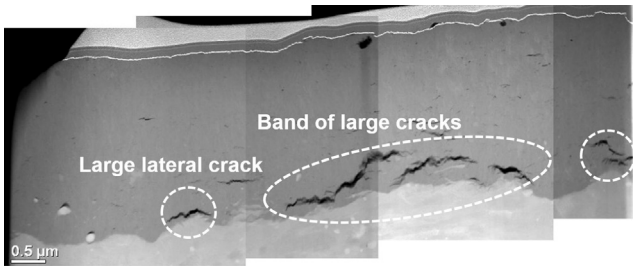

Fig. 3. Darkfield STEM image of the oxide layer of 100-day corroded sample at a high H_2 concentration (50 cc/kg) condition showing the large lateral crack and band of large cracks.

scanning electron microscopy (SEM, ZEISS SUPRA 40 (ZEISS inc., Oberkochen, Germany)) images to analyze the large area.

3. Results

3.1. Microstructure comparison by TEM analysis

A schematic diagram of the overall oxide morphology is shown in Fig. 1. The major features shown in Fig. 1 were commonly observed in all the test specimens regardless of the water chemistry conditions. Nano-size porosity and cracks along the grain boundaries were observed near the water/oxide interface. Large lateral cracks, precipitates, and columnar grains were observed near the metal/oxide interface. The metal/oxide interface had a locally irregular shape. For each region, a more detailed explanation is presented below.

Morphological variation, such as nonuniform and irregular shapes, was observed locally at the metal/oxide interface and was common to all the test samples in all the water chemistry conditions from 300 hours to 100 days. It is interesting to note that an unoxidized zirconium metal area surrounded by oxide, like an island, aggravated the interface complexity, as shown in Fig. 2. It can be inferred that the corrosion of the Zr alloy occurred locally at the metal/oxide interface. There were cracks on the top of the metal/oxide interface, as shown in Fig. 3. These cracks were commonly observed in all water chemistry conditions, and the number of cracks tended to increase with increasing time. The formation of tensile stress in the direction perpendicular to the interface and compressive stress in the direction parallel to the interface may have resulted in lateral cracks [5]. Conversely, at the valley of the interface, compressive stress was applied in all directions, and cracks did not occur [5].

It is interesting to note that all oxide layers formed in 50 cc/kg H_2 water without Zn were composed of columnar oxide grains

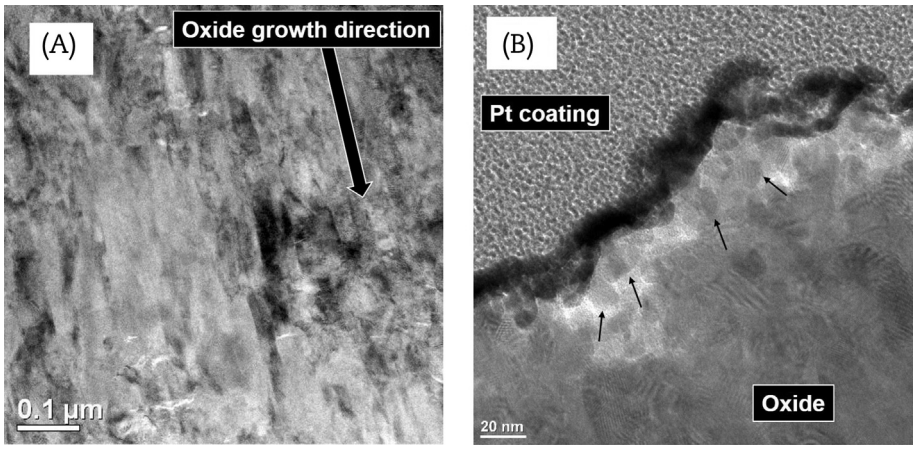

Fig. 4. (A) Brightfield STEM image of 100-day corroded sample at high hydrogen concentrations (50 cc/kg H_2 and no Zn) showing the columnar oxide grains. (B) High resolution TEM images of 50-day corroded sample in the Zn injection (30 ppb Zn and 30 cc/kg H_2) condition showing the equiaxed oxide grains (black arrows).

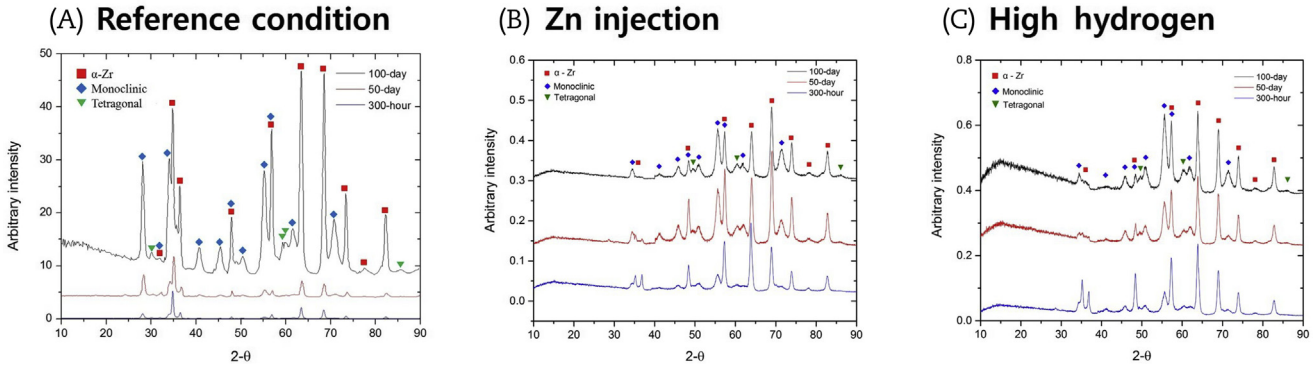

Fig. 5. Comparison of XRD spectra of 300-hour, 50-day, and 100-day corroded samples. (A) Reference condition (30 cc/kg H_2). (B) Zn injection (30 ppb Zn and 30 cc/kg H_2). (C) High H_2 concentration (50 cc/kg H_2).

(80–200 nm) near the metal/oxide interface, as shown in Fig. 4A, whereas equiaxed fine grains (10–50 nm) were dominant near the water/oxide interface after immersion in 30 cc/kg H_2 water with an addition of 30 ppb Zn, as shown in Fig. 4B. These columnar oxide grains are known to be mainly in the monoclinic phase [24–26]. Fig. 5 shows the XRD spectra of the oxide samples tested for 300 hours, 50 days, and 100 days in all the water chemistry conditions (30 cc/kg H_2, 30 ppb Zn with 30 cc/kg H_2, and 50 cc/kg H_2). The monoclinic oxide phase was predominant, but the tetragonal phase was barely detectable. Moreover, the spectra between specimens did not show a noticeable discrepancy. While α-Zr and monoclinic ZrO_2 peaks were predominant, no zirconium hydride peak was detected. One can therefore postulate that 100-day immersion in high-temperature water at 360°C may not be long enough to form zirconium hydride or the volume of zirconium hydride may have been below the detection limit of the XRD used.

Precipitates were observed near the metal/oxide interface and were commonly observed after exposure for 300 hours to 100 days in all water chemistry conditions. The precipitates were of two types: β-Nb and ZrFeNb. An example of these two precipitates is shown in Fig. 6. ZrFeNb precipitates (over 100 nm) were larger than β-Nb precipitates (10–50 nm) and were relatively less abundant. A few cracks were observed on top of the precipitates. These cracks are known to relax the stress accumulated in the oxide layer [27]. A theoretical mechanism of crack initiation on top of the precipitates was suggested by Tejland et al. [28]. As the oxidation progresses, the oxidation of the precipitate proceeds relatively slowly compared with that of the Zr matrix. Therefore, the interface between the precipitate and the oxidized Zr matrix becomes highly stressed due to the volume expansion caused by Zr oxidation. This stress can be relieved as voids or cracks are formed on the top of the precipitate or further up in the oxide.

Oxide layer thickness was measured for the reference condition (30 cc/kg H_2 and no Zn), high H_2 concentration (50 cc/kg H_2), and Zn injection (30 ppb Zn and 30 cc/kg H_2) over the different time periods. For the 300-hour and 50-day corroded samples, the oxide thickness was measured through STEM images. However, for the 100-day corroded samples with a more irregular metal/oxide interface, the oxide thickness was measured through SEM images for a wider range of measurements. Based on the measured oxide thickness data as a function of time in all water chemistry conditions, Zn injection and high H_2 concentration (50 cc/kg H_2) were found to be not likely to affect the oxide growth kinetics. Fig. 7 compares the oxide thickness measured in the reference condition (30 cc/kg H_2) with that measured with Zn injection (30 ppb Zn and 30 cc/kg H_2) and high H_2 concentration (50 cc/kg H_2). No significant difference was found in the oxide thickness for the different water chemistries. It appears that the standard deviation increased over time as the metal/oxide interface became gradually more undulating.

The oxide thickness results of the tested samples were compared with the previous data [25]. The experimental environment used by the other researchers is similar to that in this study (the only difference was in H_3BO_3 concentration), but the experiment was performed with a static autoclave. As can be seen in Table 2, the chemical composition of the samples used in the experiment was slightly different. As shown in Fig. 8, the difference

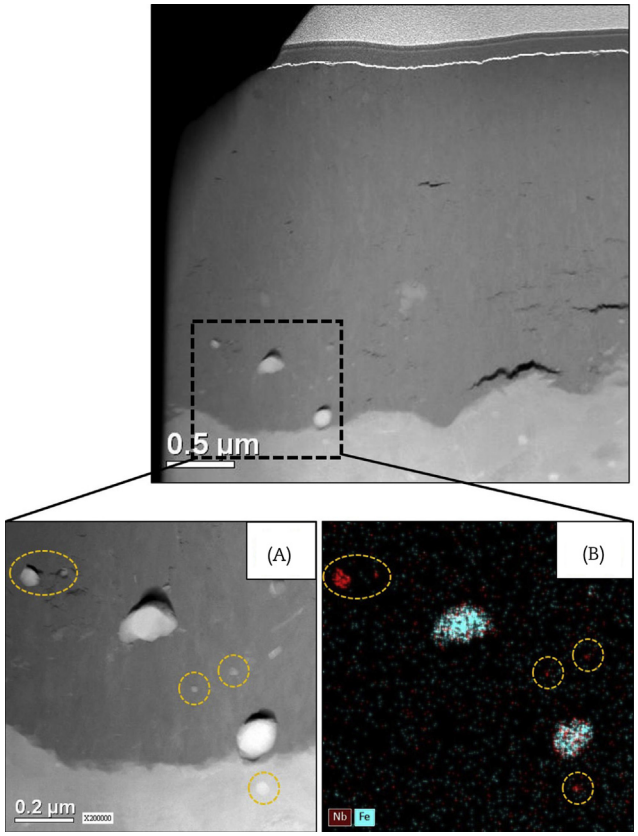

Fig. 6. (A) High angle annular darkfield STEM image of the metal/oxide interface, exhibiting precipitates in the metal and the oxide layer. (B) EDS mapping showing Nb in red and Fe in blue. β-Nb precipitates are circled, and ZrFeNb precipitates appear in mixed colors [100-day corroded sample in high H_2 concentration (50 cc/kg H_2)].

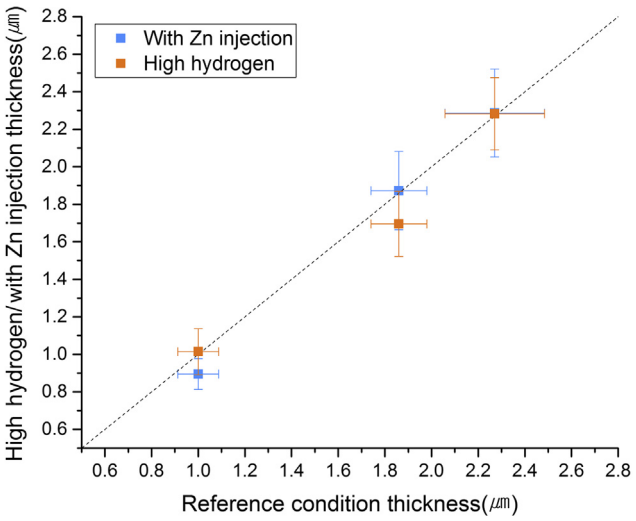

Fig. 7. Comparison of average oxide thickness and standard deviation of reference conditions (30 cc/kg H_2) and conditions involving high H_2 concentration (50 cc/kg H_2) and Zn injection (30 ppb Zn and 30 cc/kg H_2).

of oxide thickness between the two experiments was less than 0.5 μm, and the overall thickness variation tendencies were similar. Therefore, the difference in the absolute thickness value appears to be caused by the difference between the experimental conditions and the chemical compositions of the samples.

3.2. Porous region

Equiaxed grains were commonly observed near the water/oxide interface after exposure for 300 hours to 100 days in all conditions, as shown in Fig. 4B. Fig. 9 shows the interlinked porosity formed in the outer part of the oxide around the grains. This interlinked porosity existed not only at the equiaxed grain boundaries but also in the columnar grain boundaries that existed at the center of the oxide layer. Triangular microcracks were formed at the triple junctions of grains. The pore density was the highest at the top of

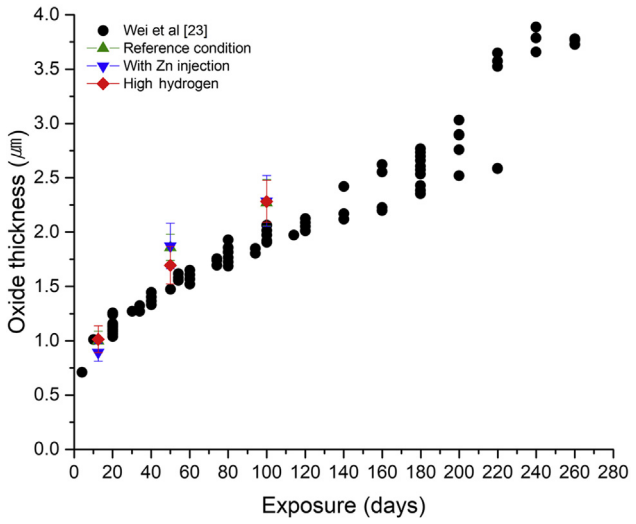

Fig. 8. Comparison of the average oxide thickness under each condition with another study [23]. The values of the oxide thickness of 100-day corroded samples were measured by SEM, and the 300-hour and 50-day corroded samples' oxide thickness were measured by STEM.

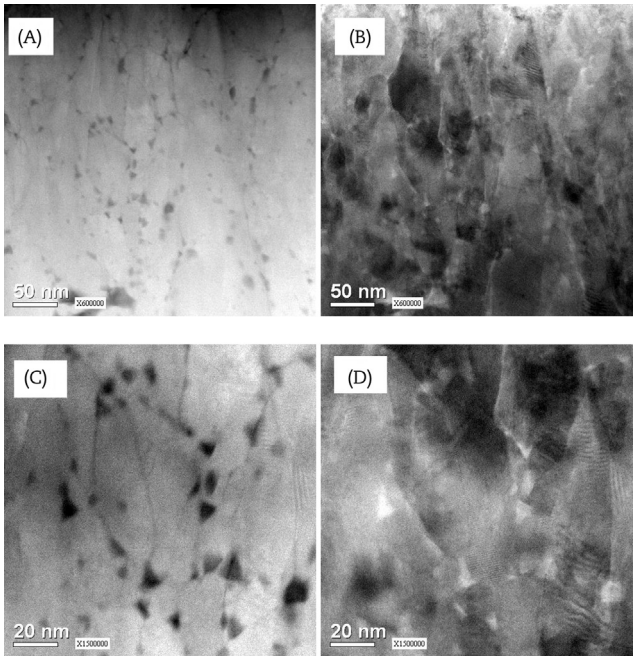

Fig. 9. (A) Darkfield STEM image of an area in the outer part of oxide showing the interlinked porosity of 50-day corroded sample in high hydrogen concentration (50 cc/kg). (B) Brightfield STEM image of (A). (C) High resolution darkfield STEM image of (A). (D) Brightfield STEM image of (C).

the oxide where corrosion began and decreased toward the metal/oxide interface. As the immersion time increased from 300 hours to 100 days, the porous region, in which porosity was observed, increased gradually, as shown in Fig. 10. It should be noted that the area indicated by a dotted square is not the exact boundary of the porous region, rather a visual guideline. The spatial and temporal variations of the porous region were not significantly dependent on the water chemistry conditions. Therefore, it can be concluded that the porosity that formed near the water/oxide interface existed in an interconnected form and that the porous region widened toward the metal/oxide interface direction as the corrosion time increased. The disconnected porosity at the metal/oxide interface changed into a continuous form (interlinked porosity) [8]. External elements could diffuse easily along the passage formed by the interlinked porosity, which affected the corrosion kinetics.

Bae et al. [29] insisted that nano-size porosity is not likely to be an artifact of focused ion beam sectioning. To prove that the observed porosity in STEM was indeed a vacant area, additional analysis was conducted. The TEM underfocusing technique was used for further analysis of the porous region. In the case of general TEM, the object was analyzed using the interference effect of the wave by employing a beam with a size of 1 mm. At this time, there was a large phase shift in this place depending on whether the object to be analyzed existed; this phase shift is called a Fresnel fringe [30]. We used the underfocusing technique to maximize the Fresnel fringe effect and clearly showed the pores observed in the STEM darkfield to be actual vacant areas. A comparison of the STEM darkfield image and the TEM underfocusing image at the same location is shown in Fig. 11. The porosity and microcracks observed in the STEM darkfield image were also observed in the TEM underfocusing image at the same location, and the pores near the water/oxide interface formed as interlinked porosity around the equiaxed grains. The density of porosity tended to decrease from the water/oxide interface toward the metal/oxide interface, as was observed in the TEM

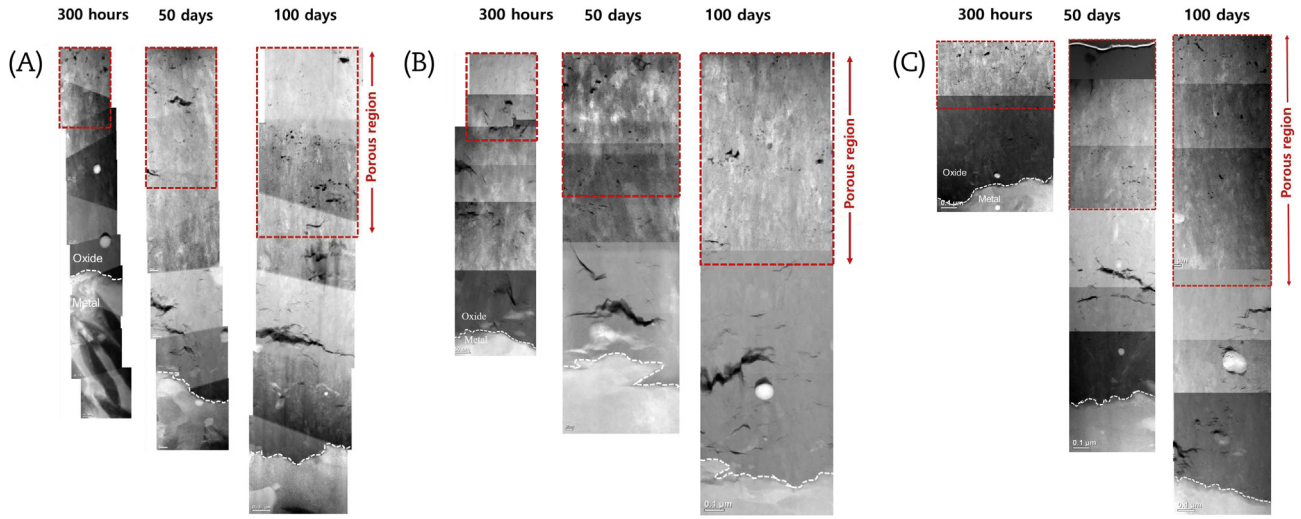

Fig. 10. Comparison of the porous regions observed in oxides of 300-hour, 50-day, and 100-day corroded samples. (A) Reference condition. (B) Zn injection condition (30 ppb Zn and 30 cc/kg H_2). (C) High H_2 concentration (50 cc/kg).

underfocusing image and in the STEM darkfield image. A short video clip showing the TEM image change with varying of the focal distance is available in the supplementary information. A comparison of two montages is shown in Fig. 12. From these comparisons, it can be confirmed that the pores observed in the STEM image from the water/oxide interface to the middle of the oxide layer (porous region) were indeed vacant areas.

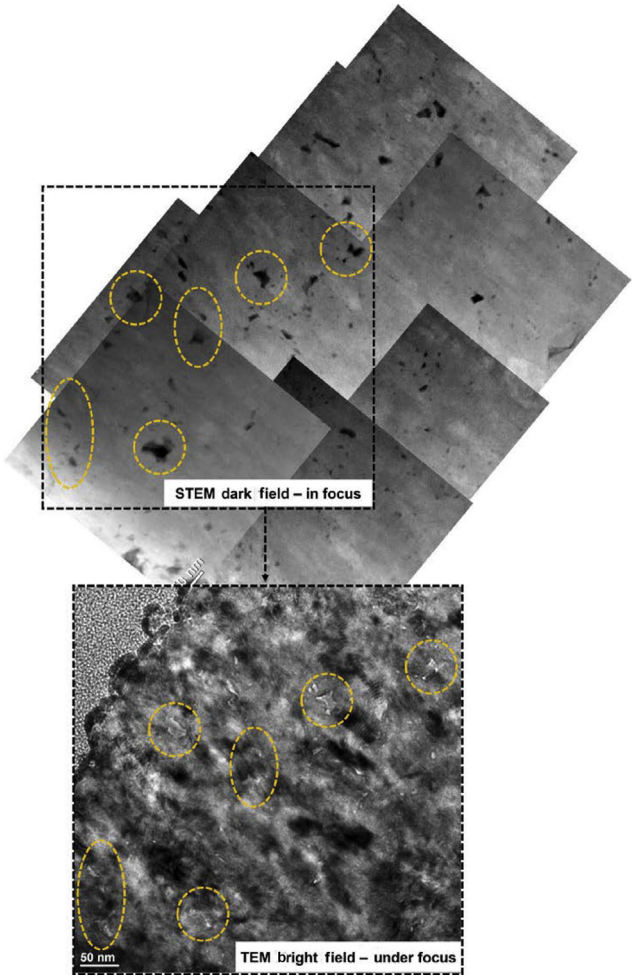

Fig. 11. Comparison of the STEM image (darkfield) and the TEM underfocusing image (brightfield) at the same locations for the 100-day corroded sample in 30 ppb Zn injection condition (Orange circles indicate the same location).

Supplementary video related to this article can be found at https://doi.org/10.1016/j.net.2017.11.009.

However, it was difficult to observe porosity near the metal/oxide interface. Similar to this study, other researchers using the TEM underfocusing technique have observed small isolated pores at the metal/oxide interface even at the pretransition stage [31]. STEM analysis of the Zr–Ti–Nb–Fe alloy (0.98% Nb, 0.21% Ti, and 0.05% Fe) with ~79 μm oxide thickness shows interlinked porosity around the grain boundary at the metal/oxide interface and at the water/oxide interface [31]. In addition, Ni et al. [31] inferred that small isolated pores of 1–3 nm initially formed near the water/oxide interface and developed into connected pores in the lateral and vertical directions. This is an important step toward the acceleration of oxide growth through the formation of an interconnected diffusion path from the water/oxide interface to the metal/oxide interface through the grain boundary.

3.3. XPS analysis

The microstructural analysis results show that the presence of 30 ppb Zn at the pretransition stage did not affect the oxide thickness. XPS surface analysis was performed to determine how Zn was incorporated on the oxide layer near the water/oxide interface. The X-ray beam was incident on the oxide surface of the test specimen after immersion for 300 hours in 30 ppb Zn and 30 cc/kg H_2 water. An approximately 400 μm × 400 μm field area was analyzed within a 10-nm depth. Fig. 13 shows the peaks of Zr3d and O1s analyzed at an approximately 10-nm depth on the surface of the sample as a ZrO_2 oxide layer. A Zn peak was also detected as ZnO (see Fig. 13B), indicating the adsorption of Zn on the oxide surface. One may postulate that Zn can penetrate into the Zr oxide through the path formed by the interlinked porosity. An XPS depth profile analysis was also performed to determine if Zn can penetrate into the oxide, but results gave no clear evidence of Zn penetration. Therefore, it can be concluded that Zn does not significantly affect the microstructure or thickness of the oxide layer in the initial oxidation process at the pretransition stage but exists only on the outermost surface layer in the form of ZnO.

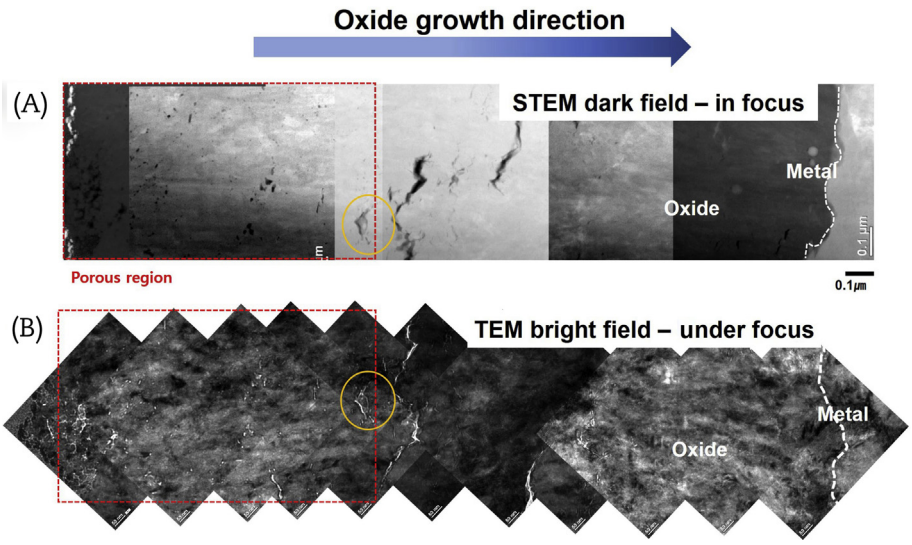

Fig. 12. Comparison of the STEM darkfield image and TEM underfocusing image. (A) STEM darkfield panorama image from water/oxide interface to metal/oxide interface in the direction of oxide growth.(B) TEM underfocusing panorama image from water/oxide interface to metal/oxide interface in the direction of oxide growth. The orange circle indicates the same location. (100-day corroded sample in 30 ppb Zn injection condition.)

4. Discussion

Unlike Zn^{2+}, H_2 can freely penetrate into the oxide. The effect of H_2 concentration (30–50 cc/kg) can be evaluated starting from the relationship between the H_2 and the porosity formation mechanisms.

The cause of the formation of these nanoscale pores at the grain boundaries is not yet clear. Several porosity formation mechanisms are available. It has been claimed that a nano pore can be formed by the Kirkendall effect [11], but this idea has been criticized by other researchers [31]. Another possible mechanism is the hydrothermal degradation of tetragonal zirconia polycrystals (3Y-TZPs). When partially stabilized 3Y-TZPs are exposed to hydrothermal conditions for relatively long periods, tetragonal to monoclinic phase transformation can occur [32]. Through this phase transformation, the strain associated with the transformation in the depth direction will be accommodated by grain boundary microcracking. The microcracking is not caused by a tetragonal to monoclinic volume change of ~4% (dilatational strain) but is the result of the shear strain accommodation produced by the formation of the first martensite plate in partially transformed grains [32]. This microcracking along the grain boundary is known to be responsible for porosity formation. The tetragonal oxide phase initially forms on zirconium alloy and then transforms to the monoclinic phase. The existence of triangular-shaped vacant areas along the grain boundary (see Fig. 9C and D) appears to support this porosity formation mechanism. Additional research, however, should be conducted to show if this grain boundary microcracking mechanism assisted by the stress-induced transformation in the hydrothermal degradation of 3Y-TZPs can be applied to zirconium alloy cladding oxidation.

The hydrothermal degradation of 3Y-TZPs gives another insight into Zr alloy oxidation from the perspective of the diffusion element in the oxide. It is generally accepted that water species in the form of OH^- ions diffuse into the material during the hydrothermal degradation of 3Y-TZPs [33–36]. Guo conducted a good review of this process [37]. When the chemical adsorption of H_2O on the ZrO_2 surface occurs, the hydroxyl ion OH^- is formed by the reaction of H_2O with O^{2-} on the ZrO_2 surface. The diffusion along the grain boundaries causes the hydroxyl ions to penetrate inside, and the hydroxyl ions fill the oxygen vacancies to form proton defects. This can trigger tetragonal to monoclinic phase transformation. In addition to OH^- ion penetration, another researcher suggested that O^{2-} and H^+ are separated and get diffused into the oxide [38,39].

Studies on Zr alloy corrosion have also suggested the presence and role of hydroxyl ion in oxide. Sundell et al. showed that significant fractions of the boundaries were decorated with hydroxide [40]. Local reduction occurs, and gaseous H_2 evolves on these hydroxide grain boundaries [41]. In this regard, a more detailed porosity formation and hydrogen pickup mechanism has been proposed [42,43]. Water species penetrate through the grain boundary of monoclinic ZrO_2 in the form of hydroxide. At the same time, hydrogen is generated by the cathodic reaction at the interface between the defect-free monoclinic ZrO_2 and the inner defect-rich tetragonal ZrO_2. The generated hydrogen, then, assists the aggregation of neutral oxygen vacancies. It is concluded that the porosity formed due to the aggregation of neutral oxygen vacancies [42,43]. Finally, it is proposed that such pore formation allows the catastrophic unwanted permeation of hydrogen into the alloys before the breakdown of the barrier oxide [42,43]. Therefore, the avalanche in the hydrogen pickup fraction was taken to reflect pore formation [42].

Therefore, the various processes of porosity formation resulting from OH^- ion diffusion have some significant implications for the effects of the high H_2 condition (50 cc/kg). If the OH^- ion was a diffusion element causing corrosion, the H_2 concentration of water did not affect the OH^- ion concentration. Therefore, the water chemistry condition that simply increased the H_2 concentration from 30 to 50 cc/kg may not have contributed to the formation of interlinked porosity through OH^- ion diffusion. Through analysis using STEM and the TEM underfocusing technique, Zn injection and high H_2 concentration were found not to significantly affect the microstructure of the oxide layer; there was no noticeable difference in the oxide thickness. Analysis of the porous region suggests that the path formed by the interlinked porosity along the grain boundary may have allowed a diffusion element to penetrate easily and ultimately trigger the transition. From the perspective of the interlinked porosity, there were no noticeable effects of Zn injection and high dissolved H_2 concentration (50 cc/kg) conditions,

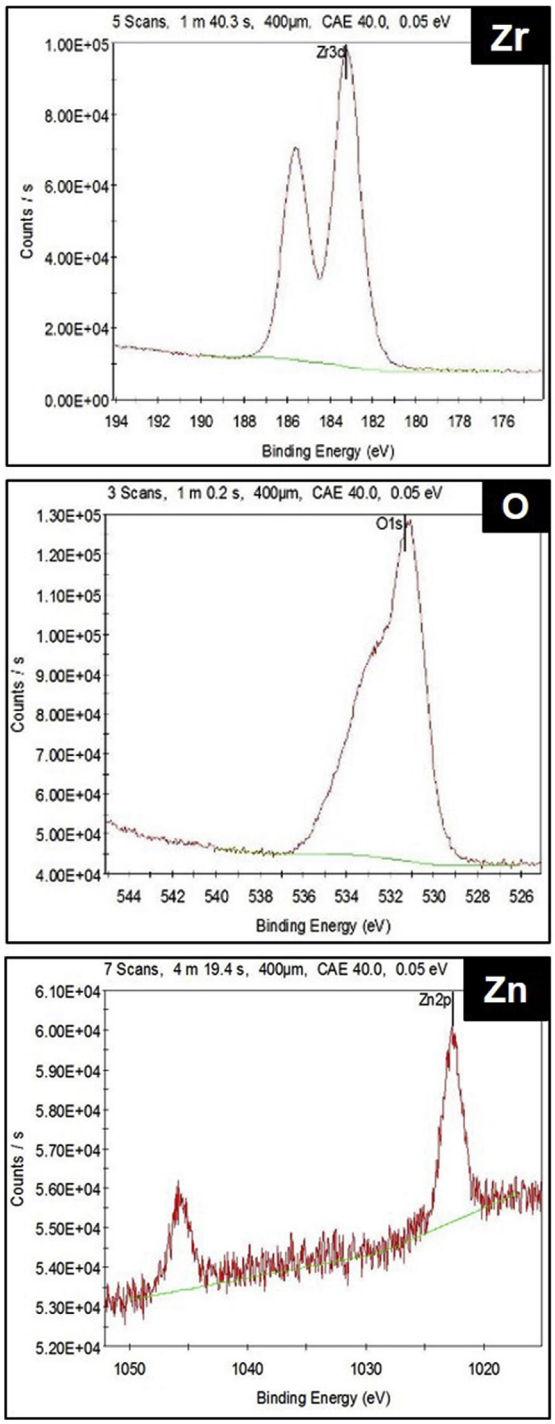

Fig. 13. XPS surface analysis on the surface of 300-hour corroded sample with 30 ppb Zn injection condition. The result showing that Zr and O peaks indicate the ZrO_2 oxide form and Zn exists in the form of ZnO on the sample surface.

suggesting that Zn gets adsorbed only on the outermost layer of Zr oxide at the water/oxide interface and is not involved in the porosity formation process. Similarly, it is unlikely that the increase in the dissolved H_2 concentration can affect the porosity formation mechanism, at least within the range of the experimental conditions we tested.

To further clarify the effect of H_2, the H_2 content in the specimens was analyzed using an ELTRA GmbH ONH-2000 element analyzer (ELTRA inc., Haan, Germany) for different cases: as-received condition, reference condition (30 cc/kg H_2), high H_2 concentration (50 cc/kg H_2), and Zn injection (30 ppb Zn and 30 cc/kg H_2). For the as-received sample, the average H_2 content was 3.8 ppm, and the standard deviation was 0.2 ppm. For the reference condition (30 cc/kg H_2), the average H_2 content and standard deviation were both 23.3 ± 1.7 ppm. The sample with high dissolved H_2 concentration (20.1 ± 0.4 ppm) or Zn injection (22.3 ± 1.2 ppm) showed H_2 content similar to that of the reference condition sample. The H_2 contents in the samples corroded for 100 days in different water chemistry conditions were not significantly different, which is consistent with the oxide thickness measurement and microstructural analysis results. However, an additional, similar corrosion test using a heated test tube with the desirable heat flux in simulated water chemistries containing various impurities (e.g., Fe/Ni oxide particulates) is necessary for a better understanding of and insight into the characteristics of oxide chemistry and microstructure in high-temperature and high-pressure water. The need for such a study is mainly due to the formation of tenacious crud on the oxide surface, which controls the growth kinetics of Zr oxide and interaction with other chemical species.

5. Conclusions

Microstructural analysis of oxide formed on Zr–Nb–Sn tube samples was performed by CS-corrected STEM, TEM, SEM, XRD, and XPS to characterize the oxide formed after immersion for various durations under simulated primary PWR water chemistry conditions with and without Zn addition and 30–50 cc/kg H_2. The main observations are as follows:

- There was no significant effect of Zn and H_2 concentrations on the microstructure of oxide formed on Zr–Nb–Sn alloy samples after exposure for 100 days (pretransition stage), although Zn was detected as ZnO on the oxide surface.
- Furthermore, based on the results of the oxide thicknesses of the samples immersed for 300 hours, 50 days, and 100 days, the presence of 30-ppb Zn or increase of H_2 from 30 to 50 cc/kg conditions did not significantly affect the oxide growth kinetics.
- Porosity along the oxide grain boundaries was analyzed using the TEM underfocusing technique, which indicates actual porous characterization. The porosity observed in the STEM darkfield image was also observed in the TEM underfocusing image, and the density of porosity decreased toward the metal/oxide interface.
- The interlinked porosity formed at the water/oxide interface widened when the porous region expanded into the metal/oxide interface direction as the oxide became thicker.
- From the perspective of OH^- ion diffusion and pore formation, the absence of any noticeable effects of Zn injection suggests that Zn was not involved in the porosity formation process. Similarly, it is unlikely that the increase in dissolved H_2 concentration can affect the porosity formation, at least within the range of the experimental conditions we tested.

Conflicts of interest

All authors have no conflicts of interest to declare.

Acknowledgments

Authors are grateful to Dr. Hoon Jang of Korea Electric Power Corporation Nuclear Fuel for analyzing the hydrogen contents. This work was supported by the Korea Institute of Energy Technology Evaluation and Planning (KETEP) and the Ministry of Trade,

Industry & Energy (MOTIE) of the Republic of Korea (No. 20168540000030), "Human Resources Program in Energy Technology" of the KETEP, granted financial resource from the MOTIE, Republic of Korea (No. 20164010201000).

References

[1] T.R. Allen, R.J.M. Konings, A.T. Motta, Corrosion of Zirconium Alloys, first ed., Elsevier Inc., 2012.
[2] A.T. Motta, M.J. Gomes da Silva, A. Yilmazbayhan, R.J. Comstock, Z. Cai, B. Lai, M. Limback, B. Kammenzind, S.W. Dean, Microstructural characterization of oxides formed on model Zr alloys using synchrotron radiation, J. ASTM Int. 5 (2008) 101257.
[3] P. Bossis, G. Lelievre, P. Barberis, X. Iltis, F. Lefebvre, Multi-scale characterization of the metal-oxide interface of zirconium alloys, in: G.P. Sabol, G.D. Moan (Eds.), Zirconium in the Nuclear Industry: Twelfth International Symposium, ASTM STP 1354, ASTM, West Conshohocken, PA, 2000, pp. 918–945.
[4] J.S. Bryner, The cyclic nature of corrosion of zircaloy-4 in 633 K water, J. Nucl. Mater. 82 (1979) 84–101.
[5] M. Parise, O. Sicardy, G. Cailletaud, Modelling of the mechanical behavior of the metal–oxide system during Zr alloy oxidation, J. Nucl. Mater. 256 (1998) 35–46.
[6] N. Ni, S. Lozano-Perez, J.M. Sykes, G.D.W. Smith, C.R.M. Grovenor, Focussed ion beam sectioning for the 3D characterisation of cracking in oxide scales formed on commercial ZIRLOTM alloys during corrosion in high temperature pressurised water, Corros. Sci. 53 (2011) 4073–4083.
[7] P. Tejland, H.O. Andrén, Origin and effect of lateral cracks in oxide scales formed on zirconium alloys, J. Nucl. Mater. 430 (2012) 64–71.
[8] N. Ni, D. Hudson, J. Wei, P. Wang, S. Lozano-Perez, G.D.W. Smith, J.M. Sykes, S.S. Yardley, K.L. Moore, S. Lyon, R.A. Cottis, M. Preuss, C.R.M. Grovenor, How the crystallography and nanoscale chemistry of the metal/oxide interface develops during the aqueous oxidation of zirconium cladding alloys, Acta Mater. 60 (2012) 7132–7149.
[9] R.A. Ploc, Mechanism of deuterium pickup in Zr-2.5Nb alloy, Mater. High Temp. 17 (2000) 29–34.
[10] B. Cox, Some thoughts on the mechanisms of in-reactor corrosion of zirconium alloys, J. Nucl. Mater. 336 (2005) 331–368.
[11] W. Gong, H. Zhang, C. Wu, H. Tian, X. Wang, The role of alloying elements in the initiation of nanoscale porosity in oxide films formed on zirconium alloys, Corros. Sci. 77 (2013) 391–396.
[12] Y. Dong, A.T. Motta, E.A. Marquis, Atom probe tomography study of alloying element distributions in Zr alloys and their oxides, J. Nucl. Mater. 442 (2013) 270–281.
[13] R. Grovenor, N. Ni, D. Hudson, S.S. Yardley, K.L. Moore, G.D.W. Smith, S. Lozano-perez, J.M. Sykes, Mechanisms of oxidation of fuel cladding alloys revealed by high resolution APT, TEM and SIMS analysis, in: Mater. Res. Soc. Symp, 2012, pp. 101–112.
[14] W. Ma, F.W. Herbert, S.D. Senanayake, B. Yildiz, Non-equilibrium oxidation states of zirconium during early stages of metal oxidation, Appl. Phys. Lett. 106 (2015) 1–6.
[15] A.T. Motta, A. Couet, R.J. Comstock, Corrosion of zirconium alloys used for nuclear fuel cladding, Annu. Rev. Mater. Res. 45 (2015) 311–343.
[16] C.C. Lin, A review of corrosion product transport and radiation field buildup in boiling water reactors, Prog. Nucl. Energy 51 (2009) 207–224.
[17] E. Chajduk, A. Bojanowska-Czajka, Corrosion mitigation in coolant systems in nuclear power plants, Prog. Nucl. Energy 88 (2016) 1–9.
[18] J.-S. Choi, S.-C. Park, K.-R. Park, H.-Y. Yang, O.-B. Yang, Effect of zinc injection on the corrosion products in nuclear fuel assembly, Nat. Sci. 5 (2013) 173–181.
[19] Electric Power Research Institute (EPRI), Pressurized Water Reactor Primary Water Chemistry Guidelines: Volume 1, Revision 5, EPRI, Palo Alto, CA, 2003, p. 1002884.
[20] D.M. Wells, R. Becker, C. Anghel, J. Iyer, J. Stevens, Out-of-reactor test of corrosion and hydrogen pickup in fuel cladding materials, in: Nuclear Plant Chemistry Conference 2014, 2014.
[21] S. Kass, The development of the Zircaloys, Corros. Zircon. Alloy 3–3 (1964) 25.
[22] H.K. Yoon, H.J. Kim, J.C. Shin, Effects of Zinc Injection on the Cladding Oxide Thickness in the Domestic Nuclear Power Plant, Transaction of the Korean Nuclear Society Autumn Meeting Gyeongju, Korea, October, 2013, pp. 24–25.
[23] J. Wei, P. Frankel, E. Polatidis, M. Blat, A. Ambard, R.J. Comstock, L. Hallstadius, D. Hudson, G.D.W. Smith, C.R.M. Grovenor, M. Klaus, R.A. Cottis, S. Lyon, M. Preuss, The effect of Sn on autoclave corrosion performance and corrosion mechanisms in Zr-Sn-Nb alloys, Acta Mater. 61 (2013) 4200–4214.
[24] H.J. Beie, A. Mitwalsky, F. Garzarolli, H. Ruhmann, H.J. Sell, Examinations of the corrosion mechanism of zirconium alloys, in: A.M. Garde, E.R. Bradley (Eds.), Zirconium in the Nuclear Industry: Tenth International Symposium, ASTM International, 100 Barr Harbor Drive, PO Box C700, West Conshohocken, PA 19428-2959, 1994, pp. 615–629.
[25] J.Y. Park, S.J. Yoo, B.K. Choi, Y.H. Jeong, Oxide microstructures of advanced Zr alloys corroded in 360°C water loop, J. Alloys Compd. 437 (2007) 274–279.
[26] A. Yilmazbayhan, E. Breval, A.T. Motta, R.J. Comstock, Transmission electron microscopy examination of oxide layers formed on Zr alloys, J. Nucl. Mater. 349 (2006) 265–281.
[27] B. De Gabory, A.T. Motta, K. Wang, Transmission electron microscopy characterization of Zircaloy-4 and ZIRLO™ oxide layers, J. Nucl. Mater. 456 (2015) 272–280.
[28] P. Tejland, M. Thuvander, H.O. Andren, S. Ciurea, T. Andersson, M. Dahlback, L. Hallstadius, H.-O. Andren, S. Ciurea, T. Andersson, M. Dahlbäck, L. Hallstadius, P. Barberis, S.W. Dean, Detailed analysis of the microstructure of the metal/oxide interface region in Zircaloy-2 after autoclave corrosion testing, J. ASTM Int. 8 (2011) 102956.
[29] H. Bae, T. Kim, J.H. Kim, C.B. Bahn, Transmission electron microscopy characterization of early pre-transition oxides formed on ZIRLOTM, Corros. Sci. Technol. 14 (2015) 301–312.
[30] M. Rühle, M. Wilkens, Defocusing contrast of cavities, Cryst. Lattice Defects 6 (3) (1975) 129–140.
[31] N. Ni, S. Lozano-Perez, M.L.L. Jenkins, C. English, G.D.W.D.W. Smith, J.M.M. Sykes, C.R.M.R.M. Grovenor, Porosity in oxides on zirconium fuel cladding alloys, and its importance in controlling oxidation rates, Scr. Mater. 62 (2010) 564–567.
[32] J.A. Muñoz-Tabares, E. Jiménez-Piqué, M. Anglada, Subsurface evaluation of hydrothermal degradation of zirconia, Acta Mater. 59 (2011) 473–484.
[33] J. Chevalier, L. Gremillard, S. Deville, Low-temperature degradation of zirconia and implications for biomedical implants, Annu. Rev. Mater. Res. 37 (2007) 1–32.
[34] H. Tsubakino, Y. Kuroda, M. Niibe, Surface relief associated with isothermal martensite in zirconia-3-mol%-yttria ceramics observed by atomic force microscopy, J. Am. Ceram. Soc. 82 (1999) 2921–2923.
[35] H. Tsubakino, K. Sonoda, R. Nozato, Martensite transformation behaviour during isothermal ageing in partially stabilized zirconia with and without alumina addition, J. Mater. Sci. Lett. 12 (1993) 196–198.
[36] W.Z. Zhu, T.C. Lei, Y. Zhou, Time-dependent tetragonal to monoclinic transition in hot-pressed zirconia stabilized with 2 mol {%} yttria, J. Mater. Sci. 28 (1993) 6479–6483.
[37] X. Guo, Property degradation of tetragonal zirconia induced by low-temperature defect reaction with water molecules, Chem. Mater. 16 (2004) 3988–3994.
[38] J. Chevalier, L. Gremillard, A.V. Virkar, D.R. Clarke, The tetragonal-monoclinic transformation in zirconia: lessons learned and future trends, J. Am. Ceram. Soc. 92 (2009) 1901–1920.
[39] T. Duong, A.M. Limarga, D.R. Clarke, Diffusion of water species in yttria-stabilized zirconia, J. Am. Ceram. Soc. 92 (2009) 2731–2737.
[40] G. Sundell, M. Thuvander, A.K. Yatim, H. Nordin, H.O. Andrén, Direct observation of hydrogen and deuterium in oxide grain boundaries in corroded Zirconium alloys, Corros. Sci. 90 (2015) 1–4.
[41] G. Sundell, M. Thuvander, H.-O. Andrén, Barrier oxide chemistry and hydrogen pick-up mechanisms in zirconium alloys, Corros. Sci. 102 (2016) 490–502.
[42] M. Lindgren, I. Panas, Oxygen vacancy formation, mobility, and hydrogen pick-up during oxidation of zirconium by water, Oxid. Met. 87 (2017) 355.
[43] M. Lindgren, C. Geers, I. Panas, Possible origin and roles of nano-porosity in ZrO_2 scales for hydrogen pick-up in Zr alloys, J. Nucl. Mater. 492 (2017) 22–31.